The South Pole Telescope

J. E. Ruhl[a], P. A. R. Ade[b], J. E. Carlstrom[c], H. M. Cho[d], T. Crawford[c], M. Dobbs[e], C. H. Greer[c], N. W. Halverson[d], W. L. Holzapfel[d], T. M. Lanting[d], A. T. Lee[d,e], J. Leong[a], E. M. Leitch[c], W. Lu[a], M. Lueker[d], J. Mehl[d], S. S. Meyer[c], J. J. Mohr[f], S. Padin [c], T. Plagge[d], C. Pryke[c], D. Schwan[d], M. K. Sharp[c], M. C. Runyan[c], H. Spieler[e], Z. Staniszewski[a] and A. A. Stark[g]

[a]Department of Physics, Case Western Reserve University, Cleveland, OH, U.S.A.;
[b]Department of Physics and Astronomy, Cardiff University, Wales, UK;
[c]Kavli Institute for Cosmological Physics, University of Chicago, Chicago, IL, U.S.A;
[d]Department of Physics, University of California, Berkeley, CA, U.S.A;
[e]Physics Division, Lawrence Berkeley National Laboratory, Berkeley, CA, U.S.A.;
[f]Department of Astronomy, University of Illinois, Urbana-Champaign, IL, U.S.A.;
[g]Harvard-Smithsonian Center for Astrophysics, Cambridge, MA, U.S.A.

ABSTRACT

A new 10 meter diameter telescope is being constructed for deployment at the NSF South Pole research station. The telescope is designed for conducting large-area millimeter and sub-millimeter wave surveys of faint, low contrast emission, as required to map primary and secondary anisotropies in the cosmic microwave background. To achieve the required sensitivity and resolution, the telescope design employs an off-axis primary with a 10 m diameter clear aperture. The full aperture and the associated optics will have a combined surface accuracy of better than 20 microns rms to allow precision operation in the submillimeter atmospheric windows. The telescope will be surrounded with a large reflecting ground screen to reduce sensitivity to thermal emission from the ground and local interference. The optics of the telescope will support a square degree field of view at 2mm wavelength and will feed a new 1000-element micro-lithographed planar bolometric array with superconducting transition-edge sensors and frequency-multiplexed readouts. The first key project will be to conduct a survey over $\sim$ 4000 degrees for galaxy clusters using the Sunyaev-Zel'dovich Effect. This survey should find many thousands of clusters with a mass selection criteria that is remarkably uniform with redshift. Armed with redshifts obtained from optical and infrared follow-up observations, it is expected that the survey will enable significant constraints to be placed on the equation of state of the dark energy.

Keywords: Radio telescopes, Millimeter- and Submillimeter-wave Techniques, Bolometric detectors, Focal plane arrays, Cosmic Microwave Background Radiation, Sunyaev-Zeldovich Effect

1. INTRODUCTION

Remarkable progress has been made in the characterization of the cosmic microwave background radiation (CMB) over the last several years. It was nearly 30 years after the initial discovery of the CMB by Penzias and Wilson in 1965[1] before small differences in its intensity were measured by COBE[2,3] and its spectrum was shown to be a blackbody to high precision.[4,5] The remarkable isotropy, precise to a part in 10^5, helped motivate the inflation theory for the origin of the universe. In the past few years, subsequent measurements of the first acoustic peak and its harmonics in the angular power spectrum[6–11] provided further support for inflation by showing the curvature of the universe was flat. They also allowed a full accounting for the matter-energy densities of the universe, finding in agreement with the analysis of Type 1a supernovae observations[12,13] that the universe is now dominated by some sort of "dark energy" that apparently is causing the expansion of the universe to accelerate. More recently the *WMAP* satellite has produced spectacular all sky maps of the temperature anisotropy yielding a highly precise measurement of the angular power spectrum up to multipoles of $\ell \sim 600$, corresponding to an angular scale of $\sim 20'$.[14] The *WMAP* data, especially combined with finer angular scale CMB anisotropy measurements made with ACBAR[15] and CBI[16] and with other probes of large scale structure have provided a

Send correspondence to J. Ruhl: E-mail: ruhl@case.edu, Telephone: 216 368 4049

high degree of confidence in the now standard cosmological model and allowed tight constraints to be placed on many of its parameters.[17]

While these measurements have led to rapid progress in our understanding of the universe, they have raised even more profound questions about the nature of dark energy and of the possibility of directly testing inflation and determining its energy scale. Remarkably, these questions can be addressed through future measurements of the CMB temperature anisotropy on fine angular scales and of the CMB polarization anisotropy on all angular scales; they form the basis of the scientific case for the South Pole Telescope (SPT) program.

Finer angular scale temperature anisotropy measurements are needed to precisely measure the angular power spectrum through the damping tail.[18] Such observations will lead to better parameter constraints and in particular allow a better characterization of the underlying primordial matter power spectrum, that in principle can be used to constrain inflationary models.[17] On angular scales of a few arcminutes and smaller, i.e., multipoles exceeding ~ 2000, the CMB anisotropy is dominated by secondary effects caused by distortions of the CMB as it passes through the universe. The largest such effect is the Sunyaev-Zeldovich Effect[19, 20] (SZE), in which the CMB photons are inverse Compton scattered by the hot intracluster gas of galaxy clusters. The SZE is a potentially powerful probe of cosmology.[21] Perhaps its most powerful use will be to enable large area, redshift independent surveys for galaxy clusters. As the growth of massive clusters is critically dependent on the underlying cosmology, the yields from such surveys can be used to set tight constraints on cosmological parameters and to investigate the nature of dark energy, i.e., by determining its equation of state.[22, 23]

Measurements of the polarization of the CMB are extremely challenging, but also have enormous potential for discovery. The intrinsic polarization of the CMB reflects the local radiation field anisotropy, specifically the local quadrupole moment of the incident radiation field, at the surface of last scattering 14 billion years ago.[24] The dominant contribution is due to Doppler shifted radiation fields arising from the acoustic oscillations at the time of last scattering. This causes the so called E-mode polarization (curl free polarization patterns on the sky) and has been detected by DASI,[25] while the temperature-polarization cross power spectrum (TE) has been detected by DASI and *WMAP*[26][*]. However, if inflation occurred in the early universe at a high-enough energy scale, a portion of the local quadrupole at last scattering will be due to primordial gravitational waves created during the inflationary epoch.[27, 28] The inflationary gravitational waves will cause both E-mode and B-mode (curl component) polarization patterns in the CMB.[29–31] While the B-mode pattern can be distinguished from the intrinsic E-mode pattern, the gravitational lensing of the CMB by large scale structure in the universe will create B-mode polarization from the intrinsic E-mode signal at a level that is higher than the inflationary B-modes for all but the most optimistic inflationary models. In this case, the only hope in recovering the inflationary B-modes from the lensing B-mode foreground lies in exploiting the different angular power spectra and their correlations with the temperature and E-mode spectra.[32, 33] The lensing polarization signal is also interesting in its own right as it can be used to trace the growth of large scale structure which in turn is sensitive to the mass of the neutrino and the equation of state of the dark energy.

This paper presents the design for a new telescope, the South Pole Telescope (SPT), that is being designed to pursue the next generation CMB temperature and polarizaton studies at the exceptional South Pole site. The telescope is designed explicitly for conducting large area, high sensitivity survey observations of the temperature and polarization of the CMB. The SPT has an off-axis 10 meter diameter aperture to provide $1'$ resolution at 2mm wavelength with exceptionally low spillover. The optics will support a one degree diameter field of view. To further reduce signals due to scattering and spillover, the entire telescope will be deployed within a large reflecting ground screen. Deployment is planned for late 2006, with first observations starting early 2007. The properties of the South Pole site are reviewed briefly in Section 2 and the telescope is discussed in Section 3.

State of the art bolometer detectors used for ground-based CMB observations are essentially background limited. In this case, the obvious path to higher sensitivity is to add more detectors. The initial SPT receiver will be dedicated for fine angular scale CMB temperature and SZE survey observations. It will consist of an array of 1000 micro-lithographed bolometers with transition edge sensors (TES) read out with a novel frequency multiplexing scheme. While a polarization-sensitive receiver is planned, only technology development funds have been obtained for it at this time. The details and status of the SZE survey receiver are outlined in Section 4.

[*]At large angular scales corresponding to the first few multipoles, the detected *WMAP* TE signal is anomalously strong indicating an early reionization of the universe.[26]

A review of the initial SPT science goals and consideration of astronomical foregrounds, atmospheric emission and the implications of these on the definition of the receiver bands and the observing strategy is given Section 5.

2. SITE

Ground based astronomical observations at mm and sub-mm wavelengths place extreme requirements on the transmission and stability of the atmosphere. Steady atmospheric emission loads the bolometric detectors and adds photon noise, reducing overall sensitivity. Fluctuations in atmospheric brightness add noise to the detector timestream data as well. For these reasons high altitude sites, preferably with stable atmospheric conditions, are needed for ground based observations such as those targeted by the SPT.

Emission from the atmosphere consists of two components, one due to "dry air" which results from the wings of oxygen lines and a second component due to water vapor. The "dry air" component is well-mixed in the atmosphere and produces a signal that is only a function of elevation, commonly removed by beam switching. Water vapor, on the other hand, exhibits considerable variations in its density. These fluctuations in water vapor density result in spatial variations in the brightness of the sky.

The South Pole lies on the Antarctic Plateau, at an altitude of 2800 m. The average atmospheric pressure in the winter is 675 millibars. In addition, the low temperature at the South Pole reduces the water vapor content of the atmosphere, lowering both atmospheric emission and fluctuations in brightness. There is a long history of measuring atmospheric properties relevant to millimeter-wave observing at the South Pole; profiles of the atmospheric temperature, pressure, and water vapor have been measured at least once a day for several decades by the South Pole meteorology office, using balloon-borne radiosondes. Schwerdtfeger[34] comprehensively reviewed the climate of the Antarctic Plateau, and found that the weather is bi-modal: 60% of the time the sky is clear with low precipitable water vapor (PWV) and weak katabatic winds (3 to 8 $\mathrm{m\,s^{-1}}$) emanating from the East Antarctic Plateau; 30% of the time is cloudy with higher PWV and stronger winds (6 to 10 $\mathrm{m\,s^{-1}}$) emanating from the Weddell Sea. Incidentally, the highest wind speed at the South Pole measured during continuous monitoring between 1957 and 1983 was only 24 m $\mathrm{s^{-1}}$, and for many months the wind speed did not exceed 12 m $\mathrm{s^{-1}}$. This low "maximum wind speed" is favorable from a telescope construction standpoint.

In addition to the meteorological measures, the millimeter and sub-millimeter opacity at the Pole has been measured by several experiments in the past decade.[35–40] The results show that deep millimeter-wave observations are possible most of the time; the median winter PWV[41] is only 0.25 mm as the air is dessicated by frigid temperatures (annual average: -49 C, minimum temperature: -82 C).

As mentioned previously, atmospheric stability is of extreme importance for our measurements. Spatial fluctuations in the brightness of the sky result in temporal noise in detector timestream data as the telescope moves the beam across the sky, or as the wind blows the atmosphere through the beam. As a function of angular scale, the power in atmospheric fluctuations is well described by a Kolmogorov spectrum and therefore falls rapidly with decreasing angular scale.

Lay and Halverson[42] used observations made with the Python experiment operating at 40 GHz to characterize atmospheric fluctuations at the South Pole during the Austral summer. They compared the results of the Python experiment with the site testing interferometer at Chajnantor[43,44] through fits to a parametric model and found that the amplitude of the sky noise at the South Pole in the summer is 10 to 50 times less than that at Chajnantor. More recently, the sky noise during the Austral winter at the South Pole was characterized in detail at frequencies of 150, 219, and 274 GHz by the ACBAR[45] experiment. Bussman *et al* used the correlation between ACBAR detectors to characterize the atmospheric fluctuation power in the presence of detector noise over the entire winter.[46] Using the water vapor opacity predicted by the modified ATM code,[47] we compared the ACBAR results with those of the Python experiment and found that the median fluctuation power during Austral winter is approximately 20 times smaller than in the summer.

As discussed in Section 5.1, we have used atmospheric noise simulations normalized by the ACBAR measurements of atmospheric fluctuation power at the South Pole to simulate SPT scan strategies in the presence of such atmospheric noise. The combination of the observed atmospheric power, wind speed, and angular scale of interest was used to compute a minimum telescope scan speed below which the atmospheric noise becomes comparable to the detector noise. The excellent atmospheric noise properties at the Pole enable quite low scanning speeds (as low as $2'$/s) with only a small impact on our science goals; this has in turn allowed the very clean SPT optical design which relies on telescope scanning (rather than a moving mirror) to move the array response across the sky.

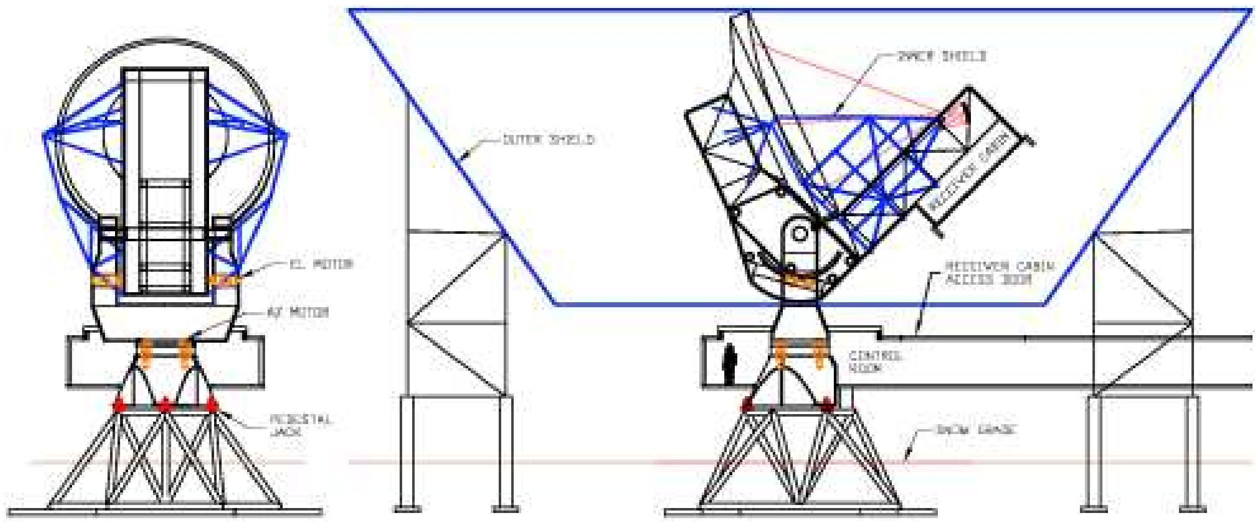

Figure 1. (Left) rear view of the SPT at elevation 0°, and (right) side view at elevation 45° with the outer ground shield.

3. TELESCOPE

The SPT will be a 10-m off-axis Gregorian telescope on an alt-az mount. The general arrangement is shown in Figure 1. The telescope design is driven by the demanding science goals (see Section 5) which require high sensitivity measurements of low contrast differential emission over a broad survey region. A large instantaneous field of view, low system noise, and stringent control of systematic offsets such as differential pickup of thermal ground emission are essential.

The telescope has key features designed to meet these needs:

1. High throughput. The SPT has a ~ 1 deg^2 diffraction-limited field of view at $\lambda = 2$ mm, so it can support cameras with several thousand detectors.
2. Low noise. The off-axis design gives low scattering, the gaps between primary panels are sealed, and the beam is well shielded. There are shields around the beam along the secondary support structure, and the entire telescope sits inside a large, stationary, conical ground shield. The primary is equipped with de-icing heaters to prevent ice from accumulating on the panels. All these lead to low optical loading on the detectors, in turn leading to high sensitivity.
3. Low offsets. The entire telescope can be chopped and scanned, so the beam does not move on the telescope mirrors. The drive supports $2^\circ \mathrm{s}^{-1}$ slew rate in elevation, $4^\circ \mathrm{s}^{-1}$ in azimuth, $4^\circ \mathrm{s}^{-2}$ acceleration in both axes, and position switching over 1° in 1.5 s (settling within 3 arcseconds of the required position). In addition, the extensive ground shielding leads to low sidelobe response in the direction of local features (eg buildings, and the horizon).
4. Submillimeter operation. The primary has a surface accuracy of 20 μm rms, and the pointing accuracy of the telescope is 1.5 arcseconds rms, so operation at wavelengths as short as 200 μm will be possible.

The telescope is being built by VertexRSI. It will be assembled and tested in the US in Jan–May 2006, prior to deployment at the South Pole in Nov 2006–Jan 2007.

3.1. Optical Design

We have chosen a classical Gregorian design for the SPT to provide flexibility for future optical configurations. In particular, this design can accommodate a chopping mirror at the pupil after the secondary, and in the classical Gregorian design (with a paraboloidal primary) the focal ratio of the telescope can be changed simply by replacing the secondary. The off-axis form was chosen because it allows a large secondary, and hence a high throughput, with low scattering and high efficiency.

Millimeter-wave Gregorian telescope designs typically have a chopper at the pupil just after the secondary. This arrangement requires re-imaging optics for low aberations over a wide-field of view.[48, 49] Unfortunately, the many reflections in these designs lead to degraded sensitivity ($\sim 1\%$ loss per warm mirror, causing extra loading on the detectors), high instrumental polarization, and chop-synchronous offsets (due to the beam moving on the secondary). Since the SPT is capable of fast scanning, we have adopted a much simpler optics configuration in which the camera is located at the Gregorian focus and there is no chopping mirror. In this compact two-mirror scheme, the stop is at the secondary (as in a typical infrared telescope) and spillover on the stop is absorbed by a cold load which surrounds the beam between the camera and the secondary.

The optical configuration of the SPT, and corresponding spot diagrams, are shown in Figure 2. The Gregorian focus is very fast – $f/1.3$, which gives maximum coupling to feedhorns of diameter $2f\lambda = 5$ mm at $\lambda = 2$ mm.[50] In this case, a 1000-element bolometer array is ~ 150 mm in diameter. The secondary is only 1 m in diameter, which is important because: (i) it sets the size of the cryostat for the cold stop; and (ii) the difficulty and cost of making a monolithic secondary increases rapidly with diameter if the secondary is larger than ~ 1 m. The Gregorian focus is stigmatic at the field center, and the geometric cross polarization is zero, i.e., the system satisfies the Dragone condition.[51] At a field radius of 0.5°, the peak cross-polar response is roughly -30 dB.

The secondary and the entire beam path from prime focus to the camera is cooled, giving low noise and stable spillover. The loss of the telescope is also low because there is just one warm reflection (at the primary) and one warm transmission (through the cryostat window near prime focus). The penalty for placing the stop at the secondary is $\sim 10\%$ degradation in resolution because the illumination pattern on the primary varies with field position. The entrance pupil of the SPT is 56 m in front of the primary, so the illumination pattern at the edge of a 1° diameter field is displaced ~ 0.5 m. Thus, the diameter of the illumination pattern must be ~ 1 m smaller than if the entrance pupil were at the primary.

Roughly 25% of the power from a $2f\lambda$ diameter, smooth-wall, conical feedhorn spills over the secondary and falls on the cold stop, so emission from the stop can cause significant loading. The temperature of the cold stop in the SPT is ~ 10 K, which gives a reasonable compromise between sensitivity loss ($\sim 5\%$ at the zenith at $\lambda = 2$ mm) and the difficulty of cooling a large mirror assembly. As shown in Figure 3, the cold stop is a conical absorbing shroud, with annular baffles near the Gregorian focus. The secondary is a lightweighted mirror (total mass ~ 15 kg), machined from an aluminum plate, with thermal cycling between machining steps to reduce deformation of the finished mirror on cooling. The secondary and stop assembly is supported by a truss attached to the cryostat wall near the prime focus port. Since the SPT must support cameras for different wavelengths, and also a polarimeter, the cryostat is split into two parts, one containing the secondary and cold stop, the other containing the detector array. The two cryostats share the same vacuum, but have independent refrigerators.

A lens immediately in front of the detector array makes the focus telecentric to improve coupling to the feedhorns. This lens is quite weak ($\sim f/10$), so it can be made from a material with fairly low refractive index, e.g., high-density polyethylene. A silicon lens would give lower loss, but a suitable anti-reflection (AR) coating is not yet available. A wide-band AR coating for the plastic lens is also not entirely straightforward. We are considering machined, profiled grooves and a multi-layer stepped-index coating made of thin sheets of laser-drilled plastic.

A key advantage of the SPT observing strategy is that the entire telescope is scanned, so the beam does not move relative to the telescope mirrors. This approach reduces offsets, but in practice there will be some scan-induced deflections and associated changes in spillover. The stability of the beam on the window and heat blocking filter near prime focus is a particular concern because the beam there has fairly sharp edges. For a filter over-sized by 10 mm in radius, a displacement of the filter changes the power at the detector by ~ 30 mK mm^{-1}. The receiver noise is $\sim 100\,\mu$K Hz$^{-1/2}$, so scan-asynchronous changes of more than a few micrometers in the position of the beam on timescales corresponding to the signal band will degrade the sensitivity. Temperature fluctuations in the cold stop also add noise, but typically will not be synchronous with the telescope scan. Again to avoid degrading sensitivity, such fluctuations much be below the level of a few $\times 10\,\mu$K Hz$^{-1/2}$ averaged over the detector readout bandwidth.

3.2. Primary

The 10-m f/0.7 SPT primary design has lightweighted machined aluminum panels (each roughly 0.75×0.5 m), mounted on a carbon fiber reinforced plastic (CFRP) back-up structure (BUS). The panels will have $\sim 8\,\mu$m rms surface accuracy. Differential contraction between the BUS and panels makes the panel gaps wider at lower ambient temperatures; if unaddressed, the effect of these gaps (emission and scattering) would increase as the atmosphere improves. At the South

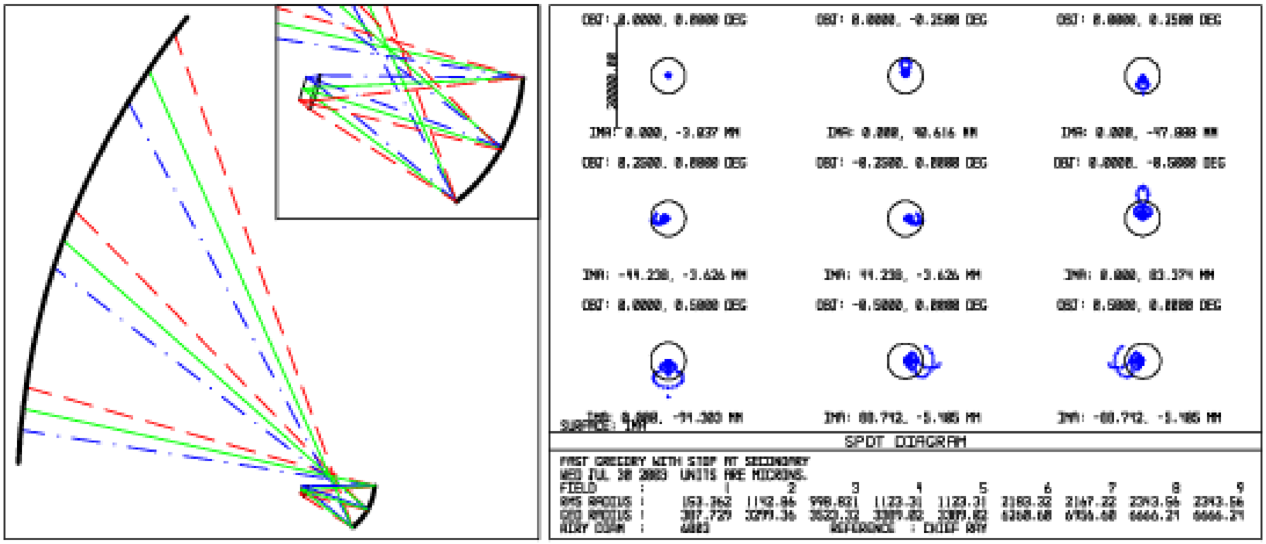

Figure 2. (Left) optical configuration of the SPT. Solid lines are the principal and marginal rays for the field center. Dashed and dot-dashed lines are for the edges of a 1° diameter field. (Right) spot diagrams. Circles show the Airy disc at $\lambda = 2$ mm.

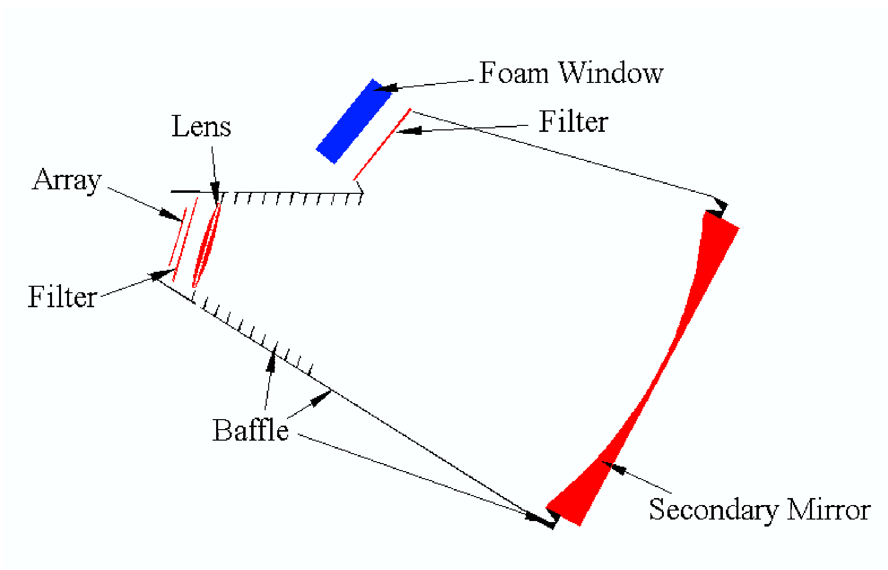

Figure 3. A cutaway view of the cold secondary and 10 K baffle optical configuration. Radiation from the primary enters through a foam vacuum window from the upper left, passing through an IR blocking filter that reduces radiative heat input on the 10 K system. The baffle is formed by two metal cones coated with a millimeter-wave absorber, with black annular rings attached to the cone wall near the 4 K lens and focal plane. For a Gaussian beam with 6 dB edge taper and a baffle emissivity of 0.5, ray-tracing of this design shows that less than 1% of the spillover power eventually exits the cryostat window.

Pole, the temperature of the primary could be as high as -10°C in summer, and to prevent the panels from touching at this temperature the panel gaps must be ~ 2 mm at -80°C. Emission from the gaps, and offsets due to small movements of the beam relative to the gaps, are a serious concern, so we plan to cover the gaps with ~ 0.1 mm thick metal strips held in place by spring fingers.

Ice on the primary panels increases the telescope emission, and causes slowly-varying offsets, and ice in the panel gaps can change the alignment of the panels. Some telescopes at the South Pole have employed manual de-icing techniques, but these are impractical for a 10-m telescope. The SPT primary will be equipped with de-icing heaters, e.g., heat blankets on the BUS, or hot air blowing between the BUS and the panels. In addition, we will select a panel surface finish that discourages ice accumulation. We are currently testing a variety of finishes at the South Pole, e.g., polished, etched, anodized, and SiO_2 coated. Initial results from this test indicate that ~ 50 $Wm^{-2}K^{-1}$ is required to heat the panels, a few K temperature rise is enough to de-ice the panels on timescales of a day or two, and the different surface finishes have roughly similar icing characteristics (but the coated surfaces are generally colder than the bare aluminum surfaces). Since de-icing can be done with a very small temperature increase, we are currently planning to run the de-icing heaters continuously at low power. This avoids the problem of having to wait for the primary to recover its profile after high-power de-icing, and reduces the peak demand on the South Pole power plant.

The SPT primary has 217 panels, each with 4 axial and 3 in-plane adjusters. The surface will be aligned initially to ~ 60 μm rms based on photogrammetry measurements, and later to 20 μm rms based on holography. Setting all the panel adjusters under the conditions at the South Pole will be a difficult task, so access to the adjusters is from inside the BUS. This is a cramped environment, but it provides protection from the wind, and allows access to the adjusters without a crane or man lift.

3.3. Ground Shields

Low noise is a critical requirement for the SPT, so the design includes several levels of shielding. The inner shield is a trough running along the secondary support as shown in Figure 1. Gaps between the inner shield, primary and secondary support are sealed with reflecting material, and the top edges of the shield and primary are rolled with a radius of a few cm to reduce scattering. The inner shield does not have de-icing heaters, so it will require occasional brushing to remove snow (through doors at the bottom of the shield near the primary).

The outer shield is an enormous inverted cone around the entire telescope. The wall angle of the cone is shallow enough to prevent radiation being trapped between the shield and the (reflective) back of the primary, so the shield does not require a floor. This makes snow removal much easier. The shield is made of 1.25-mm thick aluminum panels ~ 3 m across (the width of an LC130 aircraft) supported by a steel spaceframe. The panels are finished with a smooth epoxy phenolic coating to encourage snow shedding. A 60° wide section of the shield can be lowered to allow short, occasional observations near the horizon, e.g., calibration observations of planets, and holography using a test source on a tower. Ray tracing of the telescope with inner and outer shields shows that variations in ground pickup will be < 1mK per degree change in elevation.

3.4. Mechanical design

The SPT primary and secondary are mounted on a massive L-shaped frame on an alt-az fork mount (see Figure 1). The mount is made entirely of steel, and the CRFP BUS is attached to the steel L-frame via an Invar cone. The mount is balanced about both axes to minimize deflections in the structure and settling of the foundation, but this requires a large elevation counterweight. The azimuth bearing is at the top of a conical pedestal, which is supported by a massive spaceframe sitting on wood footings. The base of the pedestal is ~ 4 m above the ice to reduce snow drifting around the structure. Table 1 shows the masses of the major components of the SPT. Each component is designed so that it can be broken down into parts that will fit in an LC130 aircraft (which can carry about 11 metric tons).

Each axis has two pairs of torque-biased motors. The azimuth motors drive a ring gear inside the azimuth bearing, and the elevation motors drive sector gears on each side of the L-arm. The yoke and L-frame contain CFRP reference structures with displacement sensors to measure gravitational and thermal deflections of the mount. An active optical bench, which is coupled to the reference frame system, supports the secondary and camera. In this configuration, the relative positions of the secondary, lens and detector array are fixed and the entire assembly is continuously adjusted (with a control bandwidth of ~ 0.1 Hz) to maintain its position with respect to the primary. The mount also has tiltmeters above and below the azimuth bearing to measure changes in the tilt of the structure (which are included in the pointing model with a bandwidth of ~ 0.1

Table 1. Expected masses of SPT components.

Component	Mass (metric tons)
Foundation frame + footing	34
Pedestal	23
Fork	16
L-frame	77
Counterweight (lead)	73
Primary (Invar cone + BUS +panels)	18
Secondary + camera	3
Total	244

Hz). All the SPT drive components are modular, moving parts and critical electronics are in warm environments, and the drive motors, gearboxes, encoders, reference frame sensors and tiltmeters can be reached from the control room without going outside. The outside of the mount is insulated to reduce differential cooling, and interior spaces in the pedestal and fork are warmed by air from the control room.

The receiver cabin is a large ($\sim$ 6m long $\times$ 3m high $\times$ 2.5m wide) shielded and insulated room at the end of the L-frame. This provides a laboratory environment for optics and cameras, with enough space to accommodate future optical configurations with many mirrors and several optical benches. A door in the floor of the cabin mates with a hatch in the control room roof when the telescope is at the horizon (see Figure 1). Access to the cabin is also possible from outside, through the L-frame, in any telescope position.

4. RECEIVER

The statistical arrival of photons presents a fundamental limitation to the sensitivity of bolometric detectors, which has been reached for small ground-based arrays of detectors operating at mm-wavelengths.[45] The SPT science objectives require significant advances in mapping speed; to achieve this, the SPT receiver will be based on a focal plane with 1000 superconducting Transition Edge Sensor (TES) bolometers. Observations will be done sequentially in at least three frequency bands to enable spectral separation of various celestial sources. Reading out 1000 cryogenic detectors poses a technological challenge; we plan to use a SQUID-based frequency domain multiplexer readout to minimize the complexity and heat load of cold wiring. To minimize maintenance and cost of operation, the bolometer camera will be cooled by the combination of a 250 mK closed cycle refrigerator and a mechanical refrigerator that reaches $2.3\,$K without liquid cryogens. In the following sections we describe the detector array, cryogenics, readout technology and cryostat optics.

4.1. Focal Plane Array

The SPT focal-plane array will use horn-coupled spider-web bolometers with superconducting Transition-Edge Sensors (TES). Compared with conventional semiconductor-based technologies, TES detectors offer several advantages for the construction of large arrays. First, the bolometers are produced entirely by thin-film deposition and optical lithography, greatly simplifying fabrication and improving the uniformity of devices. Second, readout multiplexing technologies have been developed for TES detectors that have the potential to greatly reduce the complexity and cost of large arrays. Other benefits include high linearity and well controlled responsivity independent of base temperature and optical-loading, due to the TES's strong electrothermal feedback effect. In addition, voltage biased TES bolometers are also quite insensitive to vibration by virtue of their low impedance.

The SPT array will be assembled from 6 pie-shaped wedges each with approximately 160 bolometric detectors. Each detector consists of a small Al/Ti bi-layer TES suspended on a gold-covered Silicon Nitride spider-web absorber. We have fabricated 55 element prototype wedges of TES detectors on 4 inch wafers with high yield, like those shown in Figures 4 and 5. The individual detectors in the 55 element wedges meet the requirements for the SPT array, though the 160 element SPT wedges will need to be built on 6 inch diameter wafers.

The sensor is a bi-layer of Aluminum and Titanium, with layer thicknesses tailored to give a transition temperature of $0.5\,$K. In order for the detectors to operate with strong electrothermal feedback, the thermal conductivity needs to be

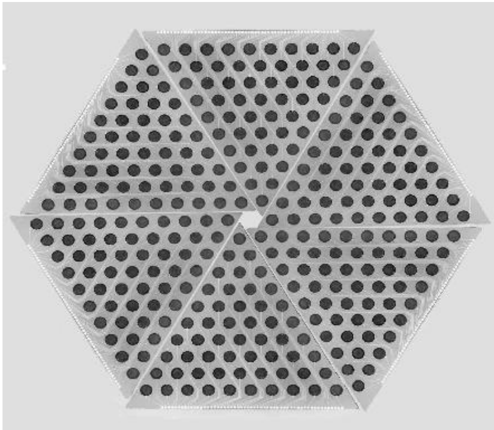

Figure 4. Montage image of a single 55-element TES spider bolometer wedge to show how an array of six identical wedges would look. The complete prototype array will have 330 bolometers and be 12 cm in diameter.

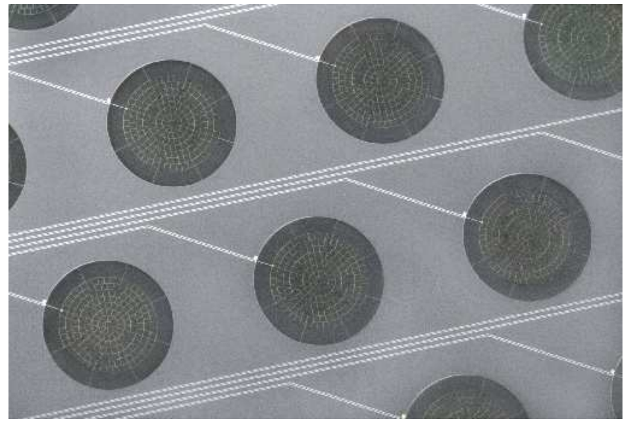

Figure 5. Close up of a 55 element bolometer wedge. The sensors are constructed with an Al/Ti proximity effect sandwich. Webs are metalized with gold for microwave absorption. Suspended spider-web absorbers are fabricated from 1 μm thick silicon nitride. The membrane is released from the front side using a gaseous xenon diflouride etch. Bolometers are 5 mm diameter with 0.5 mm long legs. Wiring layer is superconducting aluminum. This array was fabricated in the U.C. Berkeley microfabrication facility.

ν_0 (GHz)	$\Delta\nu$ (GHz)	T	P_o (pW)	G (pW/K)	$\mathrm{NET_{RJ}}$ ($\mu\mathrm{K}\sqrt{\mathrm{s}}$)	$\mathrm{NET_{CMB}}$ ($\mu\mathrm{K}\sqrt{\mathrm{s}}$)	θ_{fwhm} (arcmin)	NEFD (mJy $\sqrt{\mathrm{s}}$)
95	24	0.964	8.1	2×10^{-10}	221	278	1.58	14.6
150	38	0.982	10.8	2×10^{-10}	150	259	1.00	9.9
219	35	0.969	11.0	2×10^{-10}	184	551	0.69	12.2
274	67	0.950	24.5	4×10^{-10}	159	774	0.56	10.5
345	27	0.844	22.3	4×10^{-10}	425	4975	0.44	28.1

Table 2. Detector specifications and expected performance in each of the potential observations bands; the current baseline for the SPT is to observe in the 150, 219 and 274 GHz bands, subject to ongoing simulations of foreground removal. ν_0 is the center of the frequency band and $\Delta\nu$ is the bandwidth. T is average transmission of the atmosphere in the band. P_o is the total optical power in the band for an observation at elevation 60° and an optical efficiency of 40%. G is the thermal conductivity of the detector. $\mathrm{NET_{RJ}}$ and $\mathrm{NET_{CMB}}$ are the noise equivalent temperatures in Rayleigh-Jeans and CMB temperature units. θ_{fwhm} is the full width at half-maximum of the diffraction limited telescope beam and NEFD is the noise equivalent flux density.

chosen such that when they are subjected to the maximum expected optical load, the electrical power applied to keep the sensor in the transition region is comparable to the optical power. Unfortunately the optical background can be hard to predict and depends on the frequency band and elevation of the observations. From experience with ACBAR, we estimate the emission from cryostat optics, filters, vacuum window, and the warm primary mirror (taken to be 1% emissive) will be approximately 20 K in all frequency bands. We conservatively set the thermal conductivities G to values appropriate for 3-5 times more electrical power than the expected total optical loading during observations at elevation 60°. Even with this conservative design, the photon noise completely dominates the total noise of the detectors. Compared with NTD bolometers, the TES detectors have a much smaller contribution from Johnson noise in the sensor, and therefore somewhat lower total noise. Table 2 summarizes the design specifications and expected performance for the bolometers in each of the potential observation bands. In the 2.1 mm band, the array will image one square degree of sky to an RMS of $\Delta T_{\mathrm{cmb}} \sim 10\,\mu\mathrm{K}$ in a single hour of observation.

4.2. Cryogenics

The baseline for the SPT receiver is to use a system free of expendable cryogens, which has strong benefits for operations at the South Pole. We have assembled a test system using a Cryomech model PT-405 pulse tube cooler which provides 0.7 W of cooling power at 4.2 K and a base temperature of 2.3K. A Chase Research 3-stage Helium sorption refrigerator operates from the pulse tube cold stage. It has one stage of ^{4}He used to condense ^{3}He in two separate reservoirs, the warmer of which acts as a buffer for the coldest stage. The entire sorption refrigerator cycling process takes about 2 hours; the cold stage then maintains a steady temperature of 250 mK for 56 hours under an external heat load of 1 μW. The buffer ^{3}He stage operates at 350 mK with a cooling power of 100 μW; this stage is used to intercept heat loads from wiring and mechanical supports. We have found that vibrations from the pulse-tube cooler do not excite a substantial microphonic response in the TES bolometers, and we can achieve the baseline detector noise with the pulse-tube operating.

We have also made detailed measurements of the temperature fluctuations on each of the cryogenic stages. The fluctuations at 250 mK and 50 K are small enough to be negligible in the total detector noise budget. However, at 3 K the fluctuations from the cycling of the pulse tube can be as large as 50 mK. It will be necessary to control the temperature of the 3 K lens and IR blocking filter to a level of approximately 1 mK so that this signal is below the noise floor of the detectors. This will be achieved with a passive thermal circuit that makes use of a weak link to the large heat capacity of the cold lens. A gas gap heat switch will be used to speed the initial cooling of the lens and filter assembly from 300 K.

4.3. Receiver Optics

Due to the wide field of view of the SPT, the receiver optical elements are quite large and present considerable fabrication challenges. In Figure 3, we show a concept drawing of the cold optics box and receiver. An array of smooth wall conical feeds is used to couple the incoming radiation to the detector array. The secondary acts as a cold stop and truncates the side lobes produced by the conical feeds. Figure 6 shows a prototype 55 element conical horn array, fabricated from solid Aluminum with a set of custom ground reamers and then gold plated. The technology used to produce this prototype is easily scalable to the 160 element wedges planned for the SPT.

A relatively low-power lens is used to convert the incoming beam to the appropriate f-1.3 feed for the horns. This lens will be fabricated from polyethylene with an anti-reflection (AR) coating. The IR blocking and lowpass band-edge defining filters are constructed by bonding conductive mesh layers on polyethylene films in a heated press. The SPT optics require filters between 200-250 mm in diameter, the size of which presents a serious challenge but is within the capabilities of the fabrication facilities at Cardiff. The lower edges of the frequency bands are set by the cutoff frequency of a small section of circular waveguide behind the conical horns. The conical horn array, filters and possibly the AR-coated lens will need to be changed in order to change observation bands. We are planning to make these systems as modular as possible to facilitate rapid band changes.

As can be seen in Figure 3, the cold optics design incorporates a relatively large vacuum window. We have recently built and tested a 12” diameter window appropriate for use with the SPT. The window is constructed from a 3” thick laminate of Zotefoam PPA-30 nitrogen expanded polypropylene. It appears to be mechanically robust and holds an excellent vacuum. The total loss through the window has been measured to be less than 1.0% at 150 GHz.

4.4. Frequency Multiplexed SQUID Readout

One key to implementing an array of more than several hundred bolometers is readout multiplexing, which can dramatically reduce the heat load, the complexity of cryogenic wiring, and the cost. The SPT utilizes a frequency-domain multiplexer which requires only a single SQUID to read out a module of several bolometers.[52,53] The number of bolometers per readout module is still uncertain; eight has been demonstrated and 32 appears to be practical, so each wedge of the array will require several readout modules.

A schematic diagram showing the basic components of the readout system is shown in Figure 8. The bolometers are sine-wave biased with a constant voltage amplitude carrier, in the frequency range of 500 kHz to 1 MHz. Each bolometer within a readout module is biased at a different frequency. The sky-signal changes the bolometer resistance and amplitude modulates the bolometer current such that the signal from each bolometer is transferred to sidebands adjacent to its carrier. Thus, the signals from different bolometers within a module are uniquely positioned in frequency, so they can be summed and connected through a single wire to a SQUID amplifier.

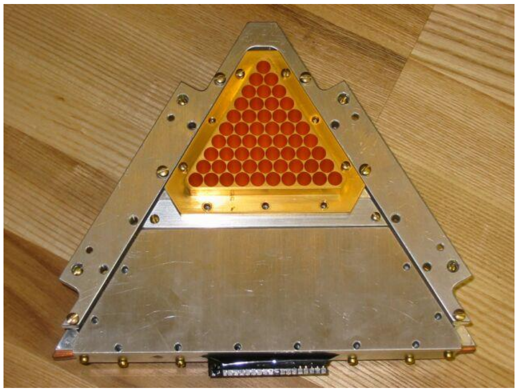

Figure 6. A 55 element horn array mounted on top of a prototype detector wedge. The SPT array will have approximately 160 horns and detectors per wedge.

Figure 7. The 16-channel oscillator/demodulator boards provide the AC bias sine-wave carriers which are sent to the bolometers. The carriers with associated sky-signal amplitude modulation are received from the bolometers and SQUID amplifiers, mixed down to base band, and digitized on-board. One oscillator/demodulator channel is required per bolometer, therefore, 60 boards in three 9U VME crates are needed for the SPT receiver.

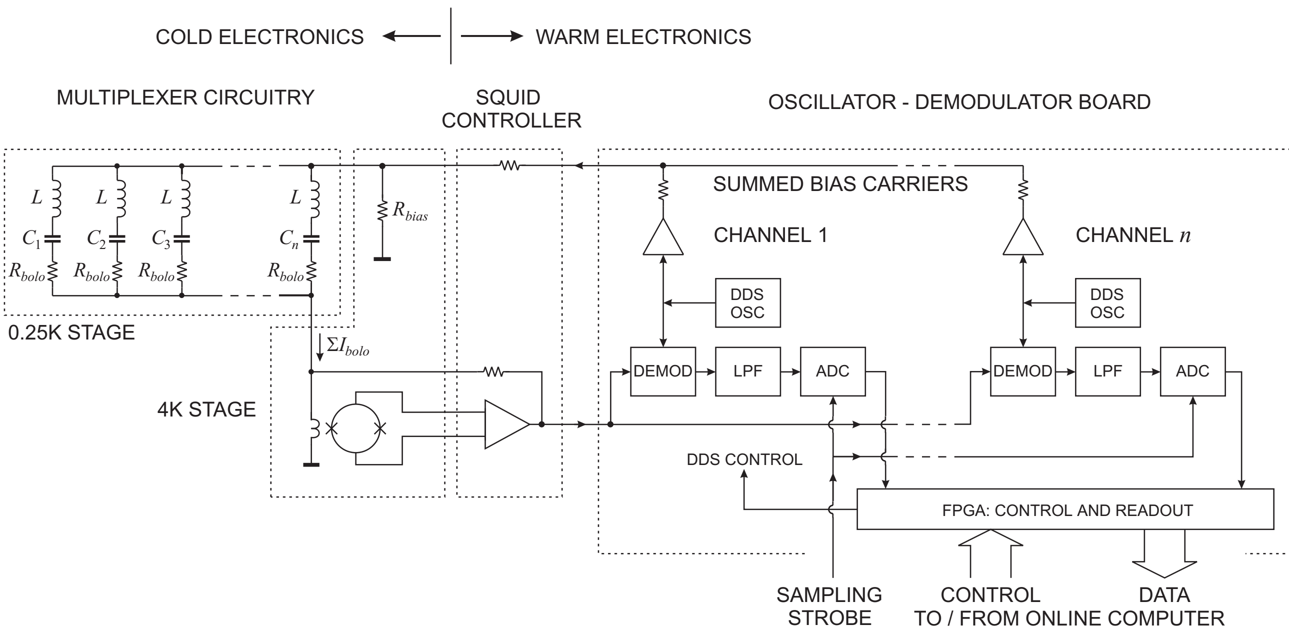

Figure 8. Schematic diagram showing the basic components of the frequency multiplexed SQUID readout system.

Each bolometer is part of a series-resonant LC circuit, which is tuned to the appropriate bias frequency. This allows the bias frequencies for all bolometers in a module to be applied through a single wire, as the tuned circuit selects the appropriate frequency for each bolometer. Thus only two wires are needed to connect the bolometers of a readout module on the 0.25 K stage to the 4 K stage on which the SQUIDs are mounted. The tuned circuits also limit the bandwidth of the bolometer's Johnson noise, which would otherwise contribute to the noise in all other channels of the module. The comb of amplitude modulated carriers at the SQUID output is transmitted to a bank of demodulators that mix the signals back down to base-band. The signals are then filtered and digitized, and all outputs in the array are sampled synchronously. Multiplexing of 8 channels has been demonstrated and the limit to the number of channels per readout module is being explored. The high-Q superconducting LC filters use lithographed inductors and commercial NP0 ceramic chip capacitors. All inductors have the same value, so the Q increases with frequency to maintain constant bandwidth. A 16 μH inductor

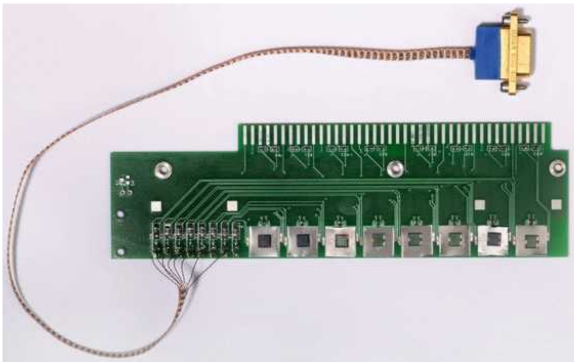

Figure 9. A printed circuit board with eight 100-element squid arrays mounted individually on top of Niobium pads. The board is mounted inside the Cryoperm shield and the Niobium films pin residual magnetic fields.

Figure 10. A prototype cryoperm shield is shown. The shield attenuates magnetic fields and provides mechanical support for the pc-board mounted SQUIDs.

together with the bolometer resistance determines the bandwidth (5 kHz), and the capacitor sets the frequency of each channel. Both the inductors and chip capacitors are compact and together occupy an area comparable to a single pixel in the array. The filters will be mounted on a board underneath the bolometer array.

The SQUID parameters must be chosen carefully to achieve the required noise performance and dynamic range. It is necessary to use SQUID devices with a small input coil to accommodate large amplitude carriers and reduce susceptibility to spurious pickup that degrades SQUID performance. This necessitates a large transimpedance of the SQUID amplifier to override the noise of the warm electronics. To meet these requirements, we utilize 100-element series array SQUID amplifiers supplied by NIST.[54] The SQUIDs are packaged on pc-boards in groups of 8 as shown in Figure 9. SQUIDs are extremely sensitive to magnetic fields and must be shielded very carefully; each board is enclosed in a cryoperm shield as shown in Figure 10. In addition, each SQUID array is individually mounted on a thin niobium film to pin the residual magnetic field. The attenuation achieved with this cryoperm/Nb shielding is better than a part-per-million at the frequencies of interest.

Maintaining constant voltage bias for the bolometers necessitates that all impedances between the bolometer and the bias resistor are much smaller than the bolometer resistance. Thus, the SQUID amplifier is operated with shunt feedback to obtain a low input impedance, while linearizing the SQUID response and extending the signal range to accommodate the high level bias carrier signals. The required gain-bandwidth product of the feedback loop requires short connections, so the SQUID controller is mounted directly on the side of the receiver cryostat. The noise of the readout system is less than 10 $\mathrm{pA}/\sqrt{\mathrm{Hz}}$ and lies well below the noise floor of the detectors planned for SPT. The system has the large dynamic range and bandwidth (1 MHz) required for frequency domain multiplexing. The SQUID controller and demodulator are computer controlled with extensive monitoring and diagnostic capabilities.

The amplified comb of carriers are passed from the SQUID controller to the oscillator/demodulator boards shown in Figure 7. Each board combines 16 demodulator channels. Since one demodulator channel is used for each bolometer, about 60 boards are required for SPT. Three 9U VME crates accommodate the readout, which is mounted in a separate rack near the cryostat. The high frequency bias carriers are generated by Direct Digital Synthesizers (DDS), which provide precise frequency and amplitude control with very low sideband noise. The same DDS that generates the bolometer bias also provides the local oscillator signal for the corresponding demodulator. The demodulator circuit utilizes a sampling demodulator with very high dynamic range [55] followed by an 8 pole low-pass anti-aliasing filter, and a 14 bit analog-to-digital converter. A field programmable gate array assembles the data from all channels on a given board and streams it to the data acquisition computer. Final testing of the oscillator/demodulator production prototypes is underway.

5. SCIENCE GOALS AND IMPLICATIONS FOR OBSERVING STRATEGY

The high sensitivity and high angular resolution of the SPT will enable several ambitious scientific programs. The initial observational program will be a large survey for galaxy clusters detected by the Sunyaev-Zel'dovich Effect (SZE). The

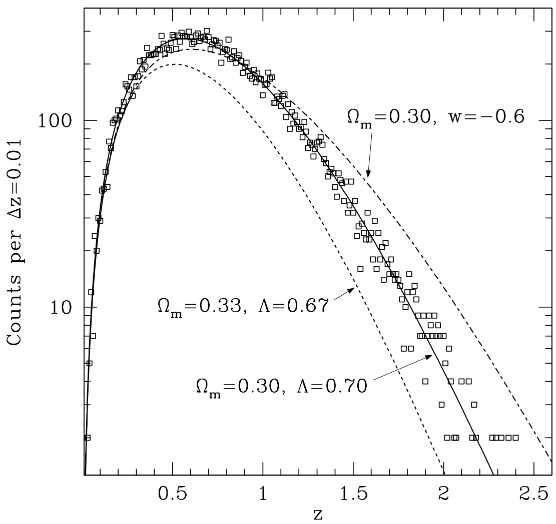

Figure 11. An illustration of the effect of cosmology on the expected number of SZE detected galaxy clusters as a function of redshift. The data points are appropriate for a 4000 square degree SPT survey with idealized sensitivity. The data points and the line passing through them were generated assuming a canonical $\Omega_M = 0.3, \Omega_\Lambda = 0.7, \sigma_8 = 1$ cosmology. The other two lines show the large effect in the expected cluster counts due to slight changes in the cosmology. The value of σ_8 was adjusted to give the same normalization for the local cluster abundance in each model. The bottom curve is for a model with more matter and correspondingly less dark energy. The top curve at shows the effect of only a change in the equation of state of the dark energy in the canonical model. (Figure courtesy of G. Holder)

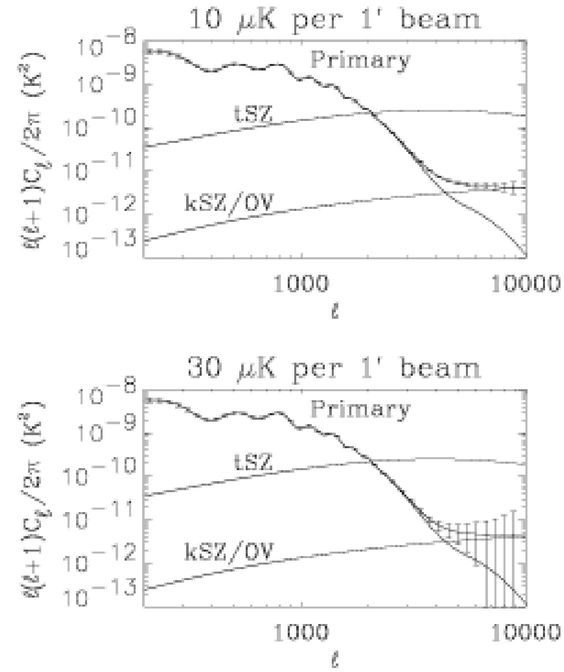

Figure 12. An illustration of the potential of the SPT to measure fine-scale CMB anisotropy. The two panels show statistical errors on the high-ℓ CMB power spectrum from 500 $\deg^2$ of sky measured at two different levels of noise per $1'$ beam. Both panels assume perfect subtraction of the thermal SZE signal and other astrophysical contaminants; achieving the required accuracy in this subtraction will be a significant challenge. (Spectra courtesy of W. Hu.)

SZE is produced when CMB photons scatter off the hot electron gas in galaxy clusters[20]; the brightness of the SZE is nearly independent of distance to the cluster, making it an ideal tool for conducting a mass-limited cluster survey.[21] The abundance of massive clusters as a function of redshift is highly sensitive to the efficiency with which structure can grow, which is in turn sensitive to the expansion history of the universe. Therefore as shown in Figure 11, the redshift evolution of the abundance of massive clusters is critically sensitive to cosmological parameters such as the amount of dark energy and its equation of state. The SPT SZE survey will enable strong constraints on the amount of and nature of dark energy in the universe.

As reviewed in Section 1, recent results from measurements of degree-scale anisotropies in the CMB have spectacularly confirmed predictions of the Hot Big Bang cosmological model, and made precise measurements of many cosmological parameters. New experiments are now focusing on characterizing the temperature fluctuations on finer angular scales, where secondary anisotropies are expected to dominate over fluctuations imprinted on the last scattering surface.[56]

As shown in Figure 12, the largest source of anisotropy at multipole values $\ell > 2000$ is expected to be the thermal SZE. Measurements of the angular power spectrum of this signal – including or removing the massive clusters detected in the SZE survey – will allow tight determinations of the parameters σ_8 and Ω_M that are complementary to those obtained with analysis of the cluster survey.[57]

The thermal SZE signal has a unique spectral signature. There is a null in the spectrum near 220 GHz, and the signal appears as a flux decrement (relative to the 2.7K background) at frequencies below this null and an increment at higher frequencies. This opens the potential for separating the SZE component from other contributions to the CMB power spectrum, such as the kinetic SZE (KSZ, due to the net motion of a cluster along the line of sight) and the Ostriker-Vishniac

(OV) effect, which is a similar effect produced by structures that are still in the linear regime. Figure 12 shows how well an ideal 500 $\deg^2$ SPT survey could measure the fine-scale KSZ/OV anisotropy signal, assuming perfect compensation for the thermal SZE signal and other astrophysical contaminants.

5.1. Atmospheric Noise

As discussed in Section 2, spatial fluctuations in atmospheric emission that are driven through the telescope beam by wind or scanning cause variations in the detector timestreams loosely referred to as "atmospheric noise". The extent to which atmospheric noise dominates instrument noise depends on the details of the site, telescope and detector array properties, frequency bands and observing strategy.

We have used a model of the fluctuations in atmospheric emission at the South Pole based on on the ACBAR observations[46] to simulate two simple methods of removing atmospheric noise for a variety of telescope scan speeds. The first method is to apply a simple high-pass filter to the detector time-stream data, removing low-frequency atmospheric (and cosmic) signals. The second method exploits the extensive overlap of beams from various detectors in the array at the height of the turbulent layer in the atmosphere.[46, 58] In practice, we fit several spatial Fourier components across the array at each time step to remove the common-mode signal from each detector's time-stream data.

Figure 13 shows results from simple binning of a simulated SPT observation of primary CMB and SZE signals using a relatively slow scan rate of $2's^{-1}$ with the data processed according to the two methods described above to remove atmospheric fluctuations. We have tuned both methods to remove the same amount of atmospheric contamination. It is clear in the figure that the common-mode analysis retains cluster information on scales beyond typical cluster radii and also retains much of the CMB information. The high-pass filter, however, removed much of the larger-scale information. Galaxy clusters are easy to detect in both cases. With these algorithms and anticipated levels of detector and atmospheric noise, the cluster mass detection limit is only $10-20\%$ higher at a scan rate of $2's^{-1}$ compared with an "infinite" scan speed. Thus we find that even relatively slow scanning of the entire telescope is a viable observing strategy, enabled by the extremely stable atmospheric conditions at the South Pole.

5.2. Frequency Band Considerations

Our choice of bands, integration time, and survey area will be driven by particular science goals and the expected contaminants. We have two main goals in this regard:

1. Minimize the effect of primary CMB and other astrophysical signals on SZE cluster detection and characterization,
2. Construct a CMB map free of thermal SZE emission (and other astrophysical contaminants), enabling a measure of the CMB power spectrum (and higher order statistics) and KSZ/OV effects at high ℓ.

Each of these goals will require broad spectral coverage; atmospheric opacity limits our choices of bands to narrow windows centered near 95, 150, 220, 270, and 350 GHz. The expected sensitivity in each band (for single-moded, unpolarized detectors) is given in Table 2. We are currently working with simulations to determine the most favorable combination of bands and integration times (per band); the results of these simulations are in large part driven by the assumptions about the foreground emission.

At the angular scales of galaxy clusters and secondary CMB anisotropies, the dominant contaminants are expected to be extragalactic point sources of two flavors: flat spectrum radio sources, and luminous dusty galaxies. With the $1'$ angular resolution of the SPT, these are difficult to separate from most cluster SZE signals simply by spatial filtering, so we turn to estimating the spectral signatures of these sources.

Synchrotron emission from galaxies and AGNs is thought to be the main mechanism for radio point source emission at frequencies less than ~ 30 GHz. The steeply falling spectrum of synchrotron emission should make these sources a negligible contaminant at 150 GHz; however, there is evidence for a population of flat or inverted-spectrum sources.[60, 61] Furthermore, there is strong evidence that radio sources are preferentially associated with clusters, thus amplifying their contamination of SZE cluster surveys.[62, 63]

The level of the radio source contamination depends strongly on the number of such flat spectrum sources (as a function of flux) and their correlation with clusters. Neither of these is yet known with enough certainty to make accurate predictions. Favorable estimates for the source density[64] and cluster correlation[63] lead to the conclusion that both the SZE survey and

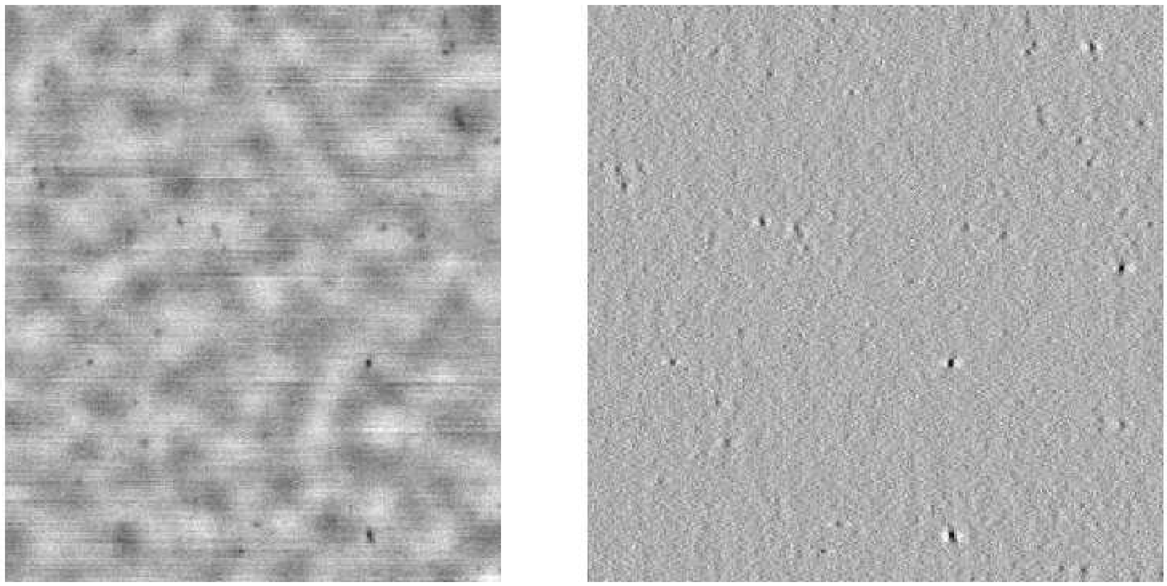

Figure 13. Two simple binned maps made from simulated array observations at 150 GHz and a scan speed of $2's^{-1}$ of a CMB-plus-SZE sky with atmospheric contamination and instrument noise with a $1/f$ knee at 0.1 Hz (SZE maps courtesy of M. White[59]). The images are 3 degrees across. The two simulated observations were filtered using different methods to achieve the same level of atmospheric rejection. **Left Panel:** results from a simulated observations in which the projection onto 16 low-frequency spatial modes across the array were subtracted at each time sample. The CMB structure is evident, as well as the cluster signals. The horizontal striping due to $1/f$ noise could be removed by a very weak high-pass filter with negligible effect on the CMB. **Right Panel:** results from a simulated observation in which each individual bolometer time-stream data was high-passed at ~ 0.3 Hz. This removes nearly all of the CMB structure, but leaves the clusters quite visible.

the CMB measurement will be unaffected by these sources. However, even the most unfavorable estimates of the source density[65] and cluster correlation[66] indicate that only a small fraction of clusters will house a radio point source that could seriously impede SZE detection at 150 GHz. We have simulated observations assuming such worst-case radio point source scenarios, and find that the contamination affects the minimum mass of clusters detected by only $10-20\%$. Our understanding of the contamination from radio point sources will be aided with new interferometric data at 100 GHz from instruments such as the SZA†.

Infrared point sources are a more likely contaminant of our survey. The SCUBA and MAMBO instruments[67,68] have detected a family of sources at 240, 350, and 670 GHz, thought to be dust-shrouded starburst galaxies that emit longward of 100 μm ($\nu < 3000$GHz) as modified blackbodies. Large numbers of detections over a range of fluxes have resulted in reasonable statistics on the sources counts versus flux at 350 GHz. Recently, rest-frame spectral energy distributions and redshifts have been determined for 73 of these objects,[69] providing a means to extrapolate the 350 GHz counts into our other candidate observing bands. The extrapolations indicate that SPT observations at 150 GHz will be contaminated by these sources. For this reason the SPT will have a high frequency "dust" channel that will be used as a monitor for these sources. The exact band or combination of bands that the SPT will use for this purpose is currently under study using a combination of Fisher-matrix-type sensitivity calculations and simulated observations.

While much work remains, the South Pole Telescope and bolometer array are currently on track for deployment to the NSF Amunsen-Scott South Pole station in late 2006. The SZE and CMB temperature anisotropy observations are scheduled to start at the beginning of the 2007 Austral winter.

†see http://astro.uchicago.edu/sza

ACKNOWLEDGMENTS

The SPT is supported by the U.S.A. National Science Foundation under Grant No. OPP-0130612. Additional support is provided by NSF Grant No. NSF PHY-0114422. Work at LBNL is supported by the Director, Office of Science, Office of High Energy and Nuclear Physics, of the U.S. Department of Energy under Contract No. DE-AC03-76SF00098. We thank VertexRSI and Raytheon Polar Support Corporation for their support of the project and Eric Chauvin for valuable contributions to the telescope design.

REFERENCES

1. A. A. Penzias and R. W. Wilson, "A Measurement of Excess Antenna Temperature at 4080 Mc/s.," *ApJ* **142**, pp. 419–421, July 1965.
2. G. F. Smoot *et al.*, "Structure in the COBE Differential Microwave Radiometer First-Year Maps," *ApJ* **396**, pp. L1–L5, 1992.
3. C. L. Bennett, A. J. Banday, K. M. Gorski, G. Hinshaw, P. Jackson, P. Keegstra, A. Kogut, G. F. Smoot, D. T. Wilkinson, and E. L. Wright, "Four-year cobe dmr cosmic microwave background observations: Maps and basic results," *ApJ* **464**, p. L1, June 1996.
4. J. C. Mather, E. S. Cheng, D. A. Cottingham, R. E. Eplee, D. J. Fixsen, T. Hewagama, R. B. Isaacman, K. A. Jensen, S. S. Meyer, P. D. Noerdlinger, S. M. Read, L. P. Rosen, R. A. Shafer, E. L. Wright, C. L. Bennett, N. W. Boggess, M. G. Hauser, T. Kelsall, S. H. Moseley, R. F. Silverberg, G. F. Smoot, R. Weiss, and D. T. Wilkinson, "Measurement of the cosmic microwave background spectrum by the COBE FIRAS instrument," *ApJ* **420**, pp. 439–444, Jan. 1994.
5. D. J. Fixsen, E. S. Cheng, J. M. Gales, J. C. Mather, R. A. Shafer, and E. L. Wright, "The Cosmic Microwave Background Spectrum from the Full COBE FIRAS Data Set," *ApJ* **473**, pp. 576–587, Dec. 1996.
6. A. D. Miller, R. Caldwell, M. J. Devlin, W. B. Dorwart, T. Herbig, M. R. Nolta, L. A. Page, J. Puchalla, E. Torbet, and H. T. Tran, "A Measurement of the Angular Power Spectrum of the Cosmic Microwave Background from l = 100 to 400," *ApJ* **524**, pp. L1–L4, Oct. 1999. astro-ph/9906421.
7. P. D. Mauskopf, P. A. R. Ade, P. de Bernardis, J. J. Bock, J. Borrill, A. Boscaleri, B. P. Crill, G. DeGasperis, G. De Troia, P. Farese, P. G. Ferreira, K. Ganga, M. Giacometti, S. Hanany, V. V. Hristov, A. Iacoangeli, A. H. Jaffe, A. E. Lange, A. T. Lee, S. Masi, A. Melchiorri, F. Melchiorri, L. Miglio, T. Montroy, C. B. Netterfield, E. Pascale, F. Piacentini, P. L. Richards, G. Romeo, J. E. Ruhl, E. Scannapieco, F. Scaramuzzi, R. Stompor, and N. Vittorio, "Measurement of a Peak in the Cosmic Microwave Background Power Spectrum from the North American Test Flight of Boomerang," *ApJ* **536**, pp. L59–L62, June 2000.
8. P. de Bernardis, P. A. R. Ade, J. J. Bock, J. R. Bond, J. Borrill, A. Boscaleri, K. Coble, B. P. Crill, G. De Gasperis, P. C. Farese, P. G. Ferreira, K. Ganga, M. Giacometti, E. Hivon, V. V. Hristov, A. Iacoangeli, A. H. Jaffe, A. E. Lange, L. Martinis, S. Masi, P. V. Mason, P. D. Mauskopf, A. Melchiorri, L. Miglio, T. Montroy, C. B. Netterfield, E. Pascale, F. Piacentini, D. Pogosyan, S. Prunet, S. Rao, G. Romeo, J. E. Ruhl, F. Scaramuzzi, D. Sforna, and N. Vittorio, "A Flat Universe from High-Resolution Maps of the Cosmic Microwave Background Radiation," *Nature* **404**, pp. 955–959, Apr. 2000. astro-ph/0004404.
9. S. Hanany, P. Ade, A. Balbi, J. Bock, J. Borrill, A. Boscaleri, P. de Bernardis, P. G. Ferreira, V. V. Hristov, A. H. Jaffe, A. E. Lange, A. T. Lee, P. D. Mauskopf, C. B. Netterfield, S. Oh, E. Pascale, B. Rabii, P. L. Richards, G. F. Smoot, R. Stompor, C. D. Winant, and J. H. P. Wu, "Maxima-1: A measurement of the cosmic microwave background anisotropy on angular scales of 10'-5°," *ApJ* **545**, pp. L5–L9, Dec. 2000. astro-ph/0005123.
10. N. W. Halverson, E. M. Leitch, C. Pryke, J. Kovac, J. E. Carlstrom, W. L. Holzapfel, M. Dragovan, J. K. Cartwright, B. S. Mason, S. Padin, T. J. Pearson, A. C. S. Readhead, and M. C. Shepherd, "Degree Angular Scale Interferometer First Results: A Measurement of the Cosmic Microwave Background Angular Power Spectrum," *ApJ* **568**, pp. 38–45, Mar. 2002. astro-ph/0104489.
11. C. B. Netterfield, P. A. R. Ade, J. J. Bock, J. R. Bond, J. Borrill, A. Boscaleri, K. Coble, C. R. Contaldi, B. P. Crill, P. de Bernardis, P. Farese, K. Ganga, M. Giacometti, E. Hivon, V. V. Hristov, A. Iacoangeli, A. H. Jaffe, W. C. Jones, A. E. Lange, L. Martinis, S. Masi, P. Mason, P. D. Mauskopf, A. Melchiorri, T. Montroy, E. Pascale, F. Piacentini, D. Pogosyan, F. Pongetti, S. Prunet, G. Romeo, J. E. Ruhl, and F. Scaramuzzi, "A Measurement by BOOMERANG of Multiple Peaks in the Angular Power Spectrum of the Cosmic Microwave Background," *ApJ* **571**, pp. 604–614, June 2002. astro-ph/0104460.

12. S. Perlmutter, G. Aldering, G. Goldhaber, R. Knop, P. Nugent, P. Castro, S. Deustua, S. Fabbro, A. Goobar, D. E. Groom, I. M. Hook, A. G. Kim, M. Kim, J. Lee, N. Nunes, R. Pain, C. Pennypacker, R. Quimby, C. Lidman, R. Ellis, M. Irwin, R. McMahon, P. Ruiz-Lapuente, N. Walton, B. Schaefer, B. Boyle, A. Filippenko, T. Matheson, A. Fruchter, N. Panagia, H. J. M. Newberg, and W. Couch, "Measurements of omega and lambda from 42 high-redshift supernovae," *ApJ* **517**, p. 565, 1999.
13. A. G. Riess, A. V. Filippenko, P. Challis, A. Clocchiatti, A. Diercks, P. M. Garnavich, R. L. Gilliland, C. J. Hogan, S. Jha, R. P. Kirshner, B. Leibundgut, M. M. Phillips, D. Reiss, B. P. Schmidt, R. A. Schommer, R. C. Smith, J. Spyromilio, C. Stubbs, N. B. Suntzeff, and J. Tonry, "Observational evidence from supernovae for an accelerating universe and a cosmological constant," *AJ* **116**, pp. 1009–1038, Sept. 1998.
14. C. L. Bennett, M. Halpern, G. Hinshaw, N. Jarosik, A. Kogut, M. Limon, S. S. Meyer, L. Page, D. N. Spergel, G. S. Tucker, E. Wollack, E. L. Wright, C. Barnes, M. R. Greason, R. S. Hill, E. Komatsu, M. R. Nolta, N. Odegard, H. V. Peiris, L. Verde, and J. L. Weiland, "First-Year Wilkinson Microwave Anisotropy Probe (WMAP) Observations: Preliminary Maps and Basic Results," *ApJS* **148**, pp. 1–27, Sept. 2003. astro-ph/0302207.
15. C. L. Kuo, P. A. R. Ade, J. J. Bock, C. Cantalupo, M. D. Daub, J. Goldstein, W. L. Holzapfel, A. E. Lange, M. Lueker, M. Newcomb, J. B. Peterson, J. Ruhl, M. C. Runyan, and E. Torbet, "High-Resolution Observations of the Cosmic Microwave Background Power Spectrum with ACBAR," *ApJ* **600**, pp. 32–51, Jan. 2004. astro-ph/0202289.
16. B. S. Mason, T. J. Pearson, A. C. S. Readhead, M. C. Shepherd, J. Sievers, P. S. Udomprasert, J. K. Cartwright, A. J. Farmer, S. Padin, S. T. Myers, J. R. Bond, C. R. Contaldi, U. Pen, S. Prunet, D. Pogosyan, J. E. Carlstrom, J. Kovac, E. M. Leitch, C. Pryke, N. W. Halverson, W. L. Holzapfel, P. Altamirano, L. Bronfman, S. Casassus, J. May, and M. Joy, "The Anisotropy of the Microwave Background to l = 3500: Deep Field Observations with the Cosmic Background Imager," *ApJ* **591**, pp. 540–555, July 2003. astro-ph/0205384.
17. D. N. Spergel, L. Verde, H. V. Peiris, E. Komatsu, M. R. Nolta, C. L. Bennett, M. Halpern, G. Hinshaw, N. Jarosik, A. Kogut, M. Limon, S. S. Meyer, L. Page, G. S. Tucker, J. L. Weiland, E. Wollack, and E. L. Wright, "First Year Wilkinson Microwave Anisotropy Probe (WMAP) Observations: Determination of Cosmological Parameters," *ApJ submitted* , Feb. 2003. astro-ph/0302209.
18. W. Hu and M. White, "The dampling tail of cosmic microwave background anisotropies," *ApJ* **479**, p. 568, 1997.
19. R. Sunyaev and Y. Zel'dovich, "The spectrum of primordial radiation, its distortions and their significance," *Comments Astrophys. Space Phys.* **2**, p. 66, 1970.
20. R. A. Sunyaev and Y. B. Zeldovich, "The Observations of Relic Radiation as a Test of the Nature of X-Ray Radiation from the Clusters of Galaxies," *Comments on Astrophysics and Space Physics* **4**, pp. 173–+, Nov. 1972.
21. J. E. Carlstrom, G. P. Holder, and E. D. Reese, "Cosmology with the Sunyaev-Zel'dovich Effect," *ARA&A* **40**, pp. 643–680, 2002.
22. G. Holder, Z. Haiman, and J. J. Mohr, "Constraints on Ω_M, Ω_Λ, and σ_8 from Galaxy Cluster Redshift Distributions," *ApJ* **560**, pp. L111–L114, Oct. 2001.
23. Z. Haiman, J. J. Mohr, and G. P. Holder, "Constraints on Cosmological Parameters from Future Galaxy Cluster Surveys," *ApJ* **553**, pp. 545–561, June 2001.
24. W. Hu and M. White, "A CMB polarization primer," *New Astronomy* **2**, pp. 323–344, 1997. astro-ph/9706147.
25. J. M. Kovac, E. M. Leitch, C. Pryke, J. E. Carlstrom, N. W. Halverson, and W. L. Holzapfel, "Detection of polarization in the cosmic microwave background using DASI," *Nature* **420**, p. 772, December 2002. astro-ph/0209478.
26. A. Kogut, D. N. Spergel, C. Barnes, C. L. Bennett, M. Halpern, G. Hinshaw, N. Jarosik, M. Limon, S. S. Meyer, L. Page, G. S. Tucker, E. Wollack, and E. L. Wright, "First-Year Wilkinson Microwave Anisotropy Probe (WMAP) Observations: Temperature-Polarization Correlation," *ApJS* **148**, pp. 161–173, Sept. 2003. astro-ph/0302213.
27. A. G. Polnarev, "Polarization and Anisotropy Induced in the Microwave Background by Cosmological Gravitational Waves," *Soviet Ast.* **29**, pp. 607–613, Dec. 1985.
28. R. Crittenden, R. L. Davis, and P. J. Steinhardt, "Polarization of the Microwave Background Due to Primordial Gravitational Waves," *ApJ* **417**, pp. L13–L16, Nov. 1993. astro-ph/9306027.
29. U. Seljak, "Measuring Polarization in the Cosmic Microwave Background," *ApJ* **482**, pp. 6–16, June 1997. astro-ph/9608131.
30. M. Kamionkowski, A. Kosowsky, and A. Stebbins, "A Probe of Primordial Gravity Waves and Vorticity," *Physical Review Letters* **78**, pp. 2058–2061, Mar. 1997. astro-ph/9609132.

31. U. Seljak and M. Zaldarriaga, “Signature of Gravity Waves in the Polarization of the Microwave Background,” *Physical Review Letters* **78**, pp. 2054–2057, Mar. 1997. astro-ph/9609169.
32. T. Okamoto and W. Hu, “Cosmic microwave background lensing reconstruction on the full sky,” *Phys. Rev. D* **67**, pp. 083002–+, Apr. 2003. astro-ph/0301031.
33. L. Knox and Y. Song, “A limit on the detectability of the energy scale of inflation,” *Physical Review Letters* **89**, p. 011303 (4 pages), 2002. astro-ph/0202286.
34. W. Schwerdtfeger, *Weather and Climate of the Antarctic*, Elsevier, Amsterdam, 1984.
35. R. A. Chamberlin and J. Bally, “The 225 GHz opacity of the South Pole sky derived from continual radiometric measurements of the sky brightness temperature,” *Applied Optics* **33**, p. 1095, 1994.
36. R. A. Chamberlin and J. Bally, “The observed relationship between the South Pole 225 GHz atmospheric opacity and the water vapor column density,” *Int. J. Infrared and Millimeter Waves* **16**, p. 907, 1995.
37. R. A. Chamberlin, A. P. Lane, and A. A. Stark, “The 492 GHz atmospheric opacity at the Geographic South Pole,” *ApJ* **476**, p. 428, 1997.
38. A. P. Lane, “Submillimeter transmission at South Pole,” in *Astrophysics from Antarctica*, G. Novak and R. H. Landsberg, eds., *ASP Conf. Ser. 141* **141**, p. 289, ASP, (San Francisco), 1998.
39. A. A. Stark, J. Bally, S. P. Balm, T. M. Bania, A. D. Bolatto, R. A. Chamberlin, G. Engargiola, M. Huang, J. G. Ingalls, K. Jacobs, J. M. Jackson, J. W. Kooi, A. P. Lane, K.-Y. Lo, R. D. Marks, C. L. Martin, D. Mumma, R. Ojha, R. Schieder, J. Staguhn, J. Stutzki, C. K. Walker, R. W. Wilson, G. A. Wright, X. Zhang, P. Zimmermann, and R. Zimmermann, “The Antarctic Submillimeter Telescope and Remote Observatory (AST/RO),” *PASP* **113**, p. 567, 2001.
40. J. B. Peterson, S. J. E. Radford, P. A. R. Ade, R. A. Chamberlin, M. J. O’Kelly, K. M. Peterson, and E. Schartman, “Stability of the submillimeter brightness of the atmosphere above Mauna Kea, Chajnantor, and the South Pole,” *PASP* **115**, pp. 383–388, 2003.
41. R. A. Chamberlin, “South Pole submillimeter sky opacity and correlations with radiosonde observations,” *J. Geophys. Res. Atmospheres* **106** (**D17**), pp. 20101–20113, 2001.
42. O. P. Lay and N. W. Halverson, “The impact of atmospheric fluctuations on degree-scale imaging of the cosmic microwave background,” *ApJ* **543**, pp. 787–798, Nov. 2000.
43. S. J. E. Radford, G. Reiland, and B. Shillue, “Site test interferometer,” *PASP* **108**, p. 441, 1996.
44. M. A. Holdaway, S. J. E. Radford, F. N. Owen, and S. M. Foster, “Fast switching phase calibration: Effectiveness at Mauna Kea and Chajnantor,” Millimeter Array Technical Memo 139, NRAO, 1995.
45. M. C. Runyan, P. A. R. Ade, R. S. Bhatia, J. J. Bock, M. D. Daub, J. H. Goldstein, C. V. Haynes, W. L. Holzapfel, C. L. Kuo, A. E. Lange, J. Leong, M. Lueker, M. Newcomb, J. B. Peterson, C. Reichardt, J. Ruhl, G. Sirbi, E. Torbet, C. Tucker, A. D. Turner, and D. Woolsey, “ACBAR: The Arcminute Cosmology Bolometer Array Receiver,” *ApJS* **149**, pp. 265–287, Dec. 2003. astro-ph/0303515.
46. M. Bussman, C. L. Kuo, and W. L. Holzapfel, “Atmsopheric noise in mm-wavelenghth bands at the South Pole,” *In Preparation* , 2004.
47. E. Serabyn and J. Pardo, “FTS measurements of submillimeter quasi-continuum atmospheric opacity terms,” in *ASP Conf. Ser. 266: Astronomical Site Evaluation in the Visible and Radio Range*, pp. 206–+, 2002.
48. A. A. Stark, “Design considerations for large detector arrays on submillimeter-wave telescopes,” in *Radio Telescopes*, H. R. Butcher, ed., **4015**, p. 434, July 2000.
49. A. A. Stark, “Meeting the optical requirements of large focal-plane arrays,” in *Proceedings of the Fourteenth Intern. Symp. on Space THz Technology*, C. Groppi, ed., 2003.
50. M. J. Griffin, J. J. Bock, and W. K. Gear, “The relative performance of filled and feedhorn-coupled focal plane architectures,” *Applied Optics* **41**(31), pp. 6543–6554, 2002. astro-ph/0205264.
51. C. Dragone, “A first-order treatment of aberrations in Cassegrainian and Gregorian antennas,” *IEEE Transactions on Antennas and Propagation* **30**(3), pp. 331–339, 1982.
52. H. Spieler, “Frequency domain multiplexing for large scale bolometer arrays,” in *Monterey Far-IR, Sub-mm and mm Detector Technology Workshop proceedings*, J. Wolf, J. Farhoomand, and C. McCreight, eds., pp. 243–249, 2002. NASA/CP-2003-21140 and LBNL-49993, http://www-library.lbl.gov/docs/LBNL/499/93/PDF/LBNL-49993.pdf.

53. T. M. Lanting, H.-M. Cho, J. Clarke, M. A. Dobbs, A. T. Lee, M. Lueker, P. L. Richards, A. D. Smith, and H. G. Spieler, "Frequency domain multiplexing for bolometer arrays," *Nuclear Instruments and Methods in Physics Research A* **520**, pp. 548–550, 2004.
54. M. Huber, P. Neil, R. Benson, D. Burns, A. Corey, C. Flynn, Y. Kitaygorodskaya, O. Massihzadeh, J. Martinis, and G. Hilton, "DC SQUID series array amplifiers with 120 MHz bandwidth (corrected)," *IEEE Transactions on Applied Superconductivity* **11**, pp. 4048–4053, 2001.
55. D. Tayloe, "Tayloe Mixer," *US Patent* **6,230,000 B1**, 2001.
56. W. Hu, N. Sugiyama, and J. Silk, "The physics of microwave background anisotropies," *Nature* **386**, pp. 37–43, 1997. astro-ph/9604166.
57. E. Komatsu and U. Seljak, "The Sunyaev-Zel'dovich angular power spectrum as a probe of cosmological parameters," *MNRAS* **336**, pp. 1256–1270, Nov. 2002. astro-ph/0205468.
58. O. P. Lay and N. W. Halverson, "The Impact of Atmospheric Fluctuations on Degree-Scale Imaging of the Cosmic Microwave Background," *ApJ* **543**, pp. 787–798, Nov. 2000. astro-ph/9905369.
59. A. E. Schulz and M. White, "Surveys of Galaxy Clusters with the Sunyaev-Zel'dovich Effect," *ApJ* **586**, pp. 723–730, Apr. 2003. astro-ph/0210667.
60. B. H. Andrew and J. D. Kraus, "Radio Sources with Flat Spectra," *ApJ* **159**, pp. L45–L50, Jan. 1970.
61. S. Trushkin, "Radio spectra of the WMAP catalog sources," *Bull.Spec.Astrophys.Obs.N.Caucasus* **55**, pp. 90–132, 2003. astro-ph/0307205.
62. J. D. H. Pilkington, "Radio sources and rich clusters of galaxies," *MNRAS* **128**, pp. 103–+, 1964.
63. A. R. Cooray, L. Grego, W. L. Holzapfel, M. Joy, and J. E. Carlstrom, "Radio Sources in Galaxy Clusters at 28.5 GHz," *AJ* **115**, p. 1388, Apr. 1998. astro-ph/9711218.
64. L. Knox, G. P. Holder, and S. E. Church, "Effects of sub-mm and radio point sources on the recovery of Sunyaev-Zeldovich galaxy cluster parameters," astro-ph/0309643.
65. M. White and S. Majumdar, "Point Sources in the Context of Future SZ Surveys," *ApJ* **602**, pp. 565–570, Feb. 2004. astro-ph/0105229.
66. M. Massardi and G. De Zotti, "Radio source contamination of the Sunyaev-Zeldovich effect in galaxy clusters," *A&Ap* . submitted, astro-ph/0405323.
67. I. Smail, R. J. Ivison, and A. W. Blain, "A deep sub-millimeter survey of lensing clusters: A new window on galaxy formation and evolution," *ApJ* **490**, p. L5, Nov. 1997.
68. E. Kreysa, H. Gemuend, J. Gromke, C. G. Haslam, L. Reichertz, E. E. Haller, J. W. Beeman, V. Hansen, A. Sievers, and R. Zylka, "Bolometer array development at the Max-Planck-Institut fuer Radioastronomie," in *Proc. SPIE Vol. 3357, p. 319-325, Advanced Technology MMW, Radio, and Terahertz Telescopes, Thomas G. Phillips; Ed.*, pp. 319–325, July 1998.
69. A. W. Blain, S. C. Chapman, I. Smail, and R. Ivison, "Accurate SEDs and selection effects for high-redshift dusty galaxies: a new hot population to discover with Spitzer?," *ApJ* . in press, astro-ph/0404438.